











# Soil Moisture Retrieval From Multipolarization SAR Data and Potential Hydrological Application

Qiang Shen , Hansheng Wang , C. K. Shum , Liming Jiang , Banghui Yang , Chaoyang Zhang ,  
Jinlong Dong , Fan Gao , Weiyu Lai , and Tiantian Liu 

**Abstract**—The high spatial-temporal variability of soil moisture necessitates monitoring at a high resolution in order to improve our understanding of Earth system processes. Current large-scale soil moistures inferred from the microwave satellites have limited spatial resolution, typically in the range of tens of kilometers. Recent studies have revealed that synthetic aperture radar (SAR) backscatter exhibits qualitative relationships with soil moisture, suggesting the potential for large-scale high-resolution mapping of soil moisture. Here, we proposed a method for directly estimating soil moisture content based on the advanced integral equation model and Mironov dielectric model. The approach involves establishing a series of semiempirical models, independent of preceding surface roughness determination, using two Envisat advanced synthetic aperture radar (ASAR) alternating polarization (AP) model precision products. We generate a time series of high-resolution soil moisture using Envisat ASAR AP data acquired from 2004 to 2011, with an uncertainty of approximately  $0.05 \text{ m}^3/\text{m}^3$ . Our soil moisture retrievals demonstrate very good agreement with European Space Agency Climate Change Initiative soil moisture products and the European Centre for Medium-Range Weather Forecasts ERA5 reanalysis hourly products, even in the absence of synchronous ground measurements. Furthermore, our study reveals good temporal coherence between drought and heavy rainfall

events, and SAR-derived soil moisture, which suggests a potential to capture heavy rainfall and drought events. We conclude that SAR-derived soil moisture is a more direct and efficient method in quantifying soil moisture at a high spatial resolution, making it more suitable for watershed scale hydrological studies.

**Index Terms**—Advanced integral equation model (AIEM), hydrology, synthetic aperture radar (SAR), soil moisture content.

## I. INTRODUCTION

THE soil moisture plays a crucial role in regulating the water resource exchange and socioeconomic activities at the watershed scale [1]. In-situ measurements are generally considered more accurate and useful for obtaining soil moisture content [2]. Over the past 70 years, various methods and instruments have been developed to improve the efficiency and accuracy of soil moisture measurements [3], [4]. Efforts have been made to establish global soil moisture networks based on in-situ measurements, although only a few networks have been implemented [5]. These networks are limited by sparse spatial sampling and short time series of soil moisture observations. In addition, the cost of maintaining in-situ measurement operations is high. To overcome these limitations and acquire soil moisture data at an appropriate resolution over large watersheds, alternative methods for soil moisture retrieval are necessary [6]. Satellite data provide a promising alternative, providing the potential for near-real-time measurement and coverage over a larger area [7], [8]. Passive or active microwave remote sensing instruments can be utilized to estimate soil moisture content based on the different relaxation frequencies of water molecules. However, the results obtained from these methods often have coarse resolutions and larger uncertainties due to the vegetation and surface roughness effects [9], [10]. Therefore, there is a need for new methods that can directly obtain soil moisture content based on advanced models, aiming to enhance our understanding of soil moisture variability and its impacts on Earth system processes [11].

In recent years, significant progress have been made in synthetic aperture radar (SAR)-based soil moisture retrieval, thanks to the availability of high-resolution multiband SAR missions, such as Envisat advanced synthetic aperture radar (ASAR) [12], Advanced Land Observing Satellite Phased Array Type L-Band Synthetic Aperture Radar (ALOS PALSAR) [13], Radarsat-1/2 [14], [15], and TerraSAR-X [16], [17]. These sensors have undergone extensive studies and evaluations to assess their capacity for soil moisture retrieval, employing both empirical and

Manuscript received 16 April 2023; revised 29 May 2023; accepted 26 June 2023. Date of publication 30 June 2023; date of current version 24 July 2023. This work was supported in part by the National Natural Science Foundation of China under Grant 41974009 and Grant 42174046, in part by the Key R&D Program of Hubei Province of China under Grant 2021CFA028, in part by the National Key R&D Program of China under Grant 2017YFA0603103, and in part by the Key Research Program of Frontier Sciences, CAS, under Grant QYZDB-SSW-DQC042. (Corresponding author: Qiang Shen.)

Qiang Shen is with the State Key Laboratory of Geodesy and Earth's Dynamics, Innovation Academy for Precision Measurement Science and Technology, Chinese Academy of Sciences, Wuhan 430077, China, also with the University of Chinese Academy of Sciences, Beijing 100049, China, and also with the Division of Geodetic Science, School of Earth Sciences, The Ohio State University, Columbus, OH 43210 USA (e-mail: c1980606@whigg.ac.cn).

Hansheng Wang, Liming Jiang, Fan Gao, Weiyu Lai, and Tiantian Liu are with the State Key Laboratory of Geodesy and Earth's Dynamics, Innovation Academy for Precision Measurement Science and Technology, Chinese Academy of Sciences, Wuhan 430077, China, and also with the University of Chinese Academy of Sciences, Beijing 100049, China (e-mail: whs@whigg.ac.cn; jlm@whigg.ac.cn; gaof@whigg.ac.cn; laiweiyu@apm.ac.cn; liutiantian21@mails.ucas.ac.cn).

C. K. Shum is with the Division of Geodetic Science, School of Earth Sciences, The Ohio State University, Columbus, OH 43210 USA (e-mail: ck.shum@outlook.com).

Banghui Yang is with the National Engineering Research Center for Geoinformatics Aerospace Information Research Institute, Chinese Academy of Sciences, Beijing 100045, China (e-mail: yangbh@aircas.ac.cn).

Chaoyang Zhang is with the Center for Space Research, University of Texas at Austin, Austin, TX 78712 USA (e-mail: cy\_zhang@austin.utexas.edu).

Jinlong Dong is with the Department of Geomatics Engineering, College of Surveying and Geo-Informatics, Shandong Jianzhu University, Jinan 250101, China (e-mail: dongjinglong20@sdjzu.edu.cn).

Digital Object Identifier 10.1109/JSTARS.2023.3291238

theoretical methods along with in-situ measurements. The Soil Moisture and Ocean Salinity (SMOS) satellite mission marks a significant milestone as the first dedicated satellite for soil moisture retrieval, providing accurate data at a relatively coarse resolution of 50 km [18]. However, this resolution limitation makes the sensor less ideal for retrieving soil moisture data at higher resolutions ranging from several meters to a kilometer.

The radar backscattering coefficient of Earth's surface is a crucial parameter measured by SAR, and it depends on various factors, such as SAR frequency, polarization, incidence angle, geometry, soil dielectric properties, and surface roughness. Several theoretical surface scattering models have been developed to analyze and simulate the echo signal received by SAR sensors, such as Kirchhoff approximation [19], geometrical optics model [20], small perturbation model [21], and integral equation model (IEM) [22]. These models are effective tools for microwave remote sensing of land cover and terrain. However, parameterizing these analytical and theoretical models becomes challenging for operational applications at high spatial resolutions and large-scale coverage, mainly due to the complexity of surface characteristics, such as vegetation canopy, topography, and soil type. Consequently, empirical parameterized inversion models have been developed, providing simplified methods to derive surface soil moisture and other parameters from microwave data. However, these models heavily rely on the validation of underlying assumptions [23].

In this study, we propose a new empirical soil moisture inversion approach inferred from the advanced integral equation model (AIEM) and Mironov dielectric model. The models have been extensively validated using C-band multipolarized SAR images in operational settings [24]. Our proposed algorithm for soil moisture retrieval is independent of surface roughness, a complex surface property that is difficult to parameterize. We apply this approach to generate high-resolution time-varying soil moisture maps using Envisat ASAR AP products acquired from 2004 to 2011, specifically covering the Beijing area. Since synchronous field measurements for the validation of the retrieved soil moisture are lacking, we compare our results with the European Space Agency (ESA) Climate Change Initiative (CCI) soil moisture products [25], [26], [27], and ERA5-Land reanalysis hourly products are used for comparison. [28]. By establishing a time series of SAR-derived soil moisture, we investigate its capability to capture extreme climate events by comparing it with precipitation measurements.

## II. METHODS AND DATA

The SAR backscattering coefficient is highly sensitive to the soil's dielectric constant, which is a function of the amount of soil's water. At present, there are many models have been developed for modeling backscattering, including semiempirical models (e.g., Oh et al. [29] and Dubois et al. [30]), analytical backscattering models, such as IEM [31]. The IEM, developed in 1992, provides an approximate solution to a pair of integral equations and offers a wider range of validity compared with existing Kirchhoff or perturbation surface fields. It allows for

a more general formulation of wave scattering problems, accommodating a broader range of roughness, soil moisture, and applicable frequencies. The AIEM is an improved version of the IEM [32], which retains all phase terms in Green's function for both single and multiple scatterings, resulting in higher accuracy in derived soil moisture content. The AIEM also introduces a transition function in Fresnel reflection coefficients to account for changes in the argument from incidence angle to the specular angle as the operational frequency or roughness increases [33], [34]. Experimental observations have shown that the AIEM outperforms semiempirical models, such as Oh et al. [29] and Dubois et al. [30], providing higher accuracy and a wider range of validity in deviations of roughness and soil moisture content [35]. The AIEM's capability and validity have been extensively validated through experimental measurements and numerical simulations, with the error decreasing as the reflection coefficients are more accurately approximated [36], [37].

The Envisat ASAR offers products for multiple polarizations, including horizontal–horizontal (HH), vertical–vertical (VV), horizontal–vertical, and vertical–horizontal. These products enable the derivation of surface parameters with high spatio-temporal resolution. With Envisat's high repeat capability, it is possible to monitor the dynamics of soil moisture change, including drying trends of the soil. In this study, the proposed semiempirical soil moisture inversion algorithms are focused on Envisat ASAR AP products with HH/VV polarization pairs and two coregistered images per acquisition from any of seven selectable swaths, providing a spatial resolution of approximately 12 m for precision products.

In theory, the backscattering coefficients ( $\sigma^0$ ) can be described as a function of soil moisture and surface parameters at different incidence angles. We summarize the backscattering coefficient as follows:

$$\sigma_{pp}^0(\theta) = f(\theta, mv, rms, cl, \varepsilon) \quad (1)$$

where  $\sigma_{pp}^0$  represents backscattering coefficient with the subscript  $pp$  standing for copolarization (HH or VV),  $f$  indicates potential relationship between dependent variables and independent variables,  $\theta$  is incidence angle,  $mv$  denotes soil moisture content,  $rms$  is referred to the root mean square (rms) of surface height,  $cl$  is correlation length, and  $\varepsilon$  is residual terms that the model cannot characterized. To simplify the number of parameters and improve the surface characterization capability, a new joint roughness parameter  $Z_s = s^2 / l$  has been proposed by Zribi [38]. By substituting  $Z_s$  into the (1), the abovementioned formula can be rewritten as follows:

$$\sigma_{pp}^0(\theta) = f(\theta, mv, Z_s, \varepsilon). \quad (2)$$

To establish a meaningful relationship between the backscattering coefficient  $\sigma^0$  and soil moisture, we created a database for AIEM simulation. The surface parameters and sensor configurations used in the simulation are provided in Table I. The Mironov dielectric model is used to simulate the relationship between soil moisture content and dielectric constant. The AIEM utilizes the following parameters to calculate the backscattering coefficient  $\sigma^0$ :

- 1) radar frequency (in GHz);

TABLE I  
RADAR, SOIL MOISTURE, AND SURFACE ROUGHNESS PARAMETERS USED IN SIMULATIONS

Radar parameters	Minimum	Maximum	Interval	Unit
Frequency	5.331 (C-band)	5.331 (C-band)	—	GHz
Incidence angle	5	75	2	degree
Soil parameters	Minimum	Maximum	Interval	Unit
cl	3	10	1	cm
RMS Height	0.3	1.0	0.1	cm
Moisture content	2	50	1	% vol.
Correlation function	exponential correlation function			

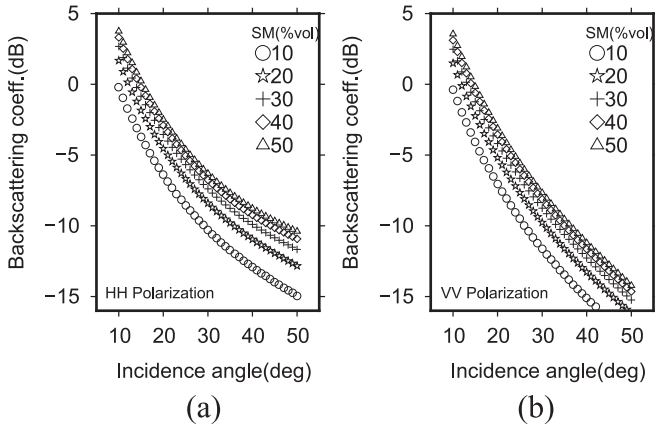


Fig. 1. AIEM simulation of backscattering coefficients as a function of incidence angle for different volumetric moisture at rms height 0.6 cm, cl 7 cm, soil moisture content varying from 10% to 50% at 10% interval for (a) HH polarization and (b) VV polarization.

- 2) incidence angle (in degrees);
- 3) rms of surface height (in cm);
- 4) cl of the surface (in cm);
- 5) soil moisture content (as a percentage of volume);
- 6) sand content of the soil (as a percentage);
- 7) clay content of the soil (as a percentage);
- 8) temperature of the soil;
- 9) soil bulk density (in  $\text{g}/\text{cm}^3$ ).

The temperature of the soil and soil bulk density were held constant at 15 °C and 1.39  $\text{g}/\text{cm}^3$ , respectively, as they have a minimal impact on the simulation [39]. The sand content and clay content of the soil were also held constant at values of 0.51 and 0.19, respectively, as they are not sensitive to the backscattering coefficient.

The backscattering coefficients  $\sigma^0$  (in HH and VV polarizations) were obtained using AIEM simulations as a function of incidence angle for different soil moisture levels ranging from 10% to 50%. The simulations were conducted with a fixed rms height of 0.6 cm and cl of 7cm, respectively (see Fig. 1). It is evident that the backscattering coefficients decrease as the incidence angle increases for all soil moisture categories. The relationship between the backscattering coefficients and incidence angle can be represented by multiple polynomials at different soil moisture values. In Fig. 2, the variation of backscattering

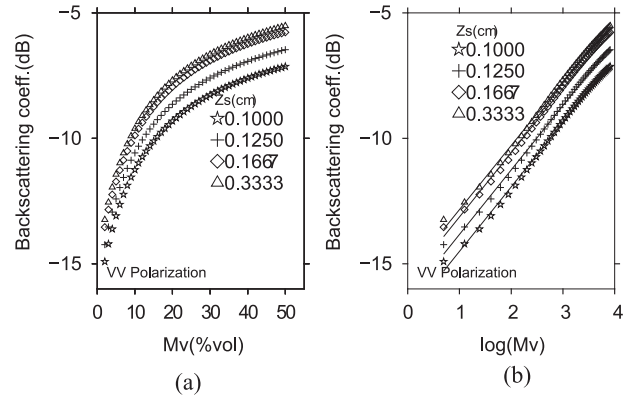


Fig. 2. AIEM simulation of backscattering coefficients (VV polarization) as a function of soil moisture (a) ( $mv$ , % vol) and (b)  $\text{Ln}(Mv)$  for different  $Zs$  (cm) values at an incidence angle 35°.

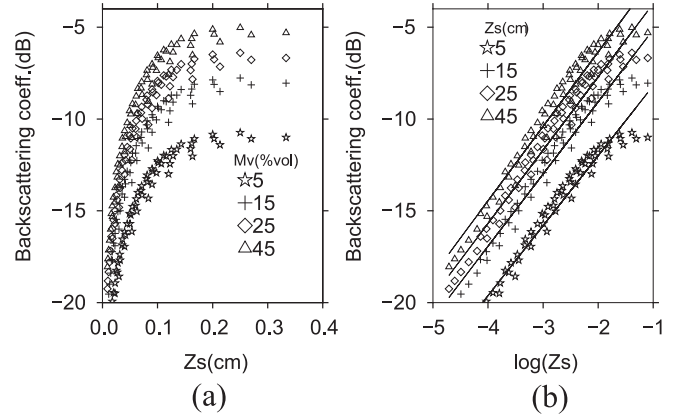


Fig. 3. AIEM simulation of backscattering coefficients (VV polarization) as function of (a)  $Zs$  (cm) and (b)  $\text{Ln}(Zs)$  for different  $mv$  (%vol) values at incidence angle 35°.

coefficient with soil moisture is shown for different surface roughness ( $Zs$ ) in VV polarization mode. A strong correlation is observed between  $\sigma^0$  and soil moisture (denoted as  $Mv$ ), with a highly linear relationship apparent between  $\sigma^0$  and the logarithm of soil moisture [ $\text{Ln}(Mv)$ ] at each  $Zs$  value ( $R^2 = 0.998$ ). The same pattern is also observed in HH polarization. Therefore, we propose the following relation:

$$\sigma_{pp}^0(\theta) = A(\theta) \text{Ln}(mv) + f(\theta, Zs) + C(\theta) \quad (3)$$

where  $A(\theta)$  and  $C(\theta)$  are coefficients dependent only on incidence angle at different polarization mode.

To accurately retrieve soil moisture, it is important to investigate and estimate the impact of surface parameters on backscattering coefficients. Fig. 3 shows the variations of backscattering coefficients (VV polarization) with  $Zs$  and  $\text{Ln}(Zs)$  for different soil moisture contents ranging from 5% to 45%, as obtained from AIEM simulation. Exponential relationships can be observed between  $\sigma^0$  and  $Zs$ , and it is appropriate to employ a linear model to describe the relationship between  $\sigma^0$  and  $\text{Ln}(Zs)$  for different soil moisture values with a high degree of confidence ( $R^2 \approx 0.97$ ), particularly for smooth and moderate surfaces. Similar findings

TABLE II  
SENSOR CONFIGURATIONS OF THE ENVISAT ASAR

Image swath	Swath width(km)	GPN <sup>1</sup>	Incidence Angle Range	WCN <sup>2</sup>
IS1	105	187–292	15.0–22.9	-20.4
IS2	105	242–347	19.2–26.7	-20.6
IS3	82	337–419	26.0–31.4	-20.6
IS4	88	412–500	31.0–36.3	-19.4
IS5	64	490–555	35.8–39.4	-20.2
IS6	70	550–620	39.1–42.8	-22.0
IS7	56	615–671	42.5–45.2	-21.9

<sup>1</sup>: GPN: ground position from nadir (km).

<sup>2</sup>: WCN: worst-case noise equivalent sigma zero.

hold for HH polarization as well. Therefore, an empirical model linking  $\sigma^0$  and  $Z_s$  can be formulated as follows:

$$\sigma_{pp}^0(\theta) = B(\theta) \text{Ln}(Z_s) + f(\theta, mv) + C(\theta) \quad (4)$$

where coefficients  $B(\theta)$  and  $C(\theta)$  depend only on the incidence angle in the corresponding polarization mode denoted by pp, and  $f(\theta, mv)$  represents a potential relation between  $mv$  and backscattering coefficients. The relationship between the backscattering coefficients and soil moisture and roughness can be expressed as follows in both HH and VV polarizations, by combining expressions (3) and (4).

$$\sigma_{pp}^0(\theta) = A(\theta) \text{Ln}(mv) + B(\theta) \text{Ln}(Z_s) + C(\theta). \quad (5)$$

### III. ESTIMATION OF MODEL PARAMETERS

To obtain a practical operational model, practical expressions for the coefficients  $A(\theta)$ ,  $B(\theta)$ , and  $C(\theta)$  in terms of incidence angle  $\theta$  were derived. Backscattering coefficients in HH and VV polarizations were calculated using AIEM at each incidence angle ranging from  $10^\circ$  to  $50^\circ$ , covering all image swaths of Envisat ASAR (see Table II). Nonlinear regression algorithms were employed to extract the coefficients  $A(\theta)$ ,  $B(\theta)$ , and  $C(\theta)$  at each incidence angle based on (5). The detailed information of each coefficient in HH and VV polarizations can be found in Tables III and IV, respectively. It can be observed that the nonlinear regressions are consistent with the original simulation data ( $R^2 > 0.9$ ), except for small incidence angles ( $\theta < 21^\circ$ ), corresponding to IS1 image swath (see Table II). Moreover, the accuracy of the model predictions increases with incidence angle. When the incidence angle increases to  $35^\circ$ , the difference between the model and data becomes negligible. To establish the relationship between each coefficient ( $A(\theta)$ ,  $B(\theta)$ ,  $C(\theta)$ ) and incidence angle in radians, polynomials were used. There is a strong correlation between the coefficients and angles ( $R^2 = 0.999$ ), and the relationship can be approximated using cubic polynomials. However, it should be noted that there is a very small difference between the polynomial predictions and the simulation data at small incidence angles. The specific polynomial expressions for the coefficients  $A(\theta)$ ,  $B(\theta)$ , and  $C(\theta)$

TABLE III  
FITTED COEFFICIENTS  $A(\theta)$ ,  $B(\theta)$ ,  $C(\theta)$ , AND  $R^2$  FOR HH POLARIZATION OF C-BAND

$\theta$	$A(\theta)$	$B(\theta)$	$C(\theta)$	$R^2$	$\theta$	$A(\theta)$	$B(\theta)$	$C(\theta)$	$R^2$
10	2.4555	0.5170	5.5559	0.65	31	2.4481	3.6213	3.9080	0.96
11	2.4553	0.7752	5.5652	0.68	32	2.4462	3.7112	3.8098	0.96
12	2.4552	1.0129	5.5529	0.71	33	2.4439	3.7990	3.7129	0.96
13	2.4551	1.2325	5.5227	0.74	34	2.4413	3.8850	3.6173	0.96
14	2.4551	1.4364	5.4778	0.77	35	2.4382	3.9693	3.5229	0.97
15	2.4551	1.6263	5.4208	0.79	36	2.4347	4.0520	3.4299	0.97
16	2.4552	1.8039	5.3536	0.82	37	2.4307	4.1334	3.3380	0.97
17	2.4552	1.9705	5.2780	0.84	38	2.4261	4.2135	3.2472	0.97
18	2.4553	2.1274	5.1957	0.85	39	2.4210	4.2925	3.1572	0.97
19	2.4553	2.2756	5.1077	0.87	40	2.4152	4.3703	3.0679	0.97
20	2.4553	2.4159	5.0154	0.88	41	2.4087	4.4471	2.9790	0.97
21	2.4553	2.5492	4.9196	0.89	42	2.4015	4.5230	2.8902	0.97
22	2.4552	2.6762	4.8211	0.90	43	2.3935	4.5979	2.8012	0.97
23	2.4550	2.7976	4.7207	0.91	44	2.3847	4.6720	2.7115	0.97
24	2.4547	2.9138	4.6191	0.92	45	2.3749	4.7450	2.6206	0.97
25	2.4543	3.0255	4.5167	0.93	46	2.3642	4.8172	2.5281	0.97
26	2.4538	3.1330	4.4140	0.94	47	2.3524	4.8884	2.4332	0.97
27	2.4531	3.2368	4.3115	0.94	48	2.3395	4.9586	2.3355	0.97
28	2.4522	3.3372	4.2094	0.95	49	2.3255	5.0276	2.2340	0.96
29	2.4511	3.4346	4.1079	0.95	50	2.3103	5.0955	2.1280	0.96
30	2.4497	3.5292	4.0074	0.95					

TABLE IV  
FITTED COEFFICIENTS  $A(\theta)$ ,  $B(\theta)$ ,  $C(\theta)$ , AND  $R^2$  FOR VV POLARIZATION OF C-BAND

$\theta$	$A(\theta)$	$B(\theta)$	$C(\theta)$	$R^2$	$\theta$	$A(\theta)$	$B(\theta)$	$C(\theta)$	$R^2$
10	2.4655	0.4584	5.6081	.66	31	2.5009	3.0362	3.8651	0.97
11	2.4659	0.7042	5.6194	.69	32	2.5064	3.0873	3.7582	0.97
12	2.4662	0.9280	5.6082	0.72	33	2.5125	3.1351	3.6527	0.98
13	2.4666	1.1326	5.5783	0.75	34	2.5193	3.1800	3.5486	0.98
14	2.4669	1.3202	5.5329	0.78	35	2.5268	3.2219	3.4461	0.98
15	2.4673	1.4926	5.4746	0.80	36	2.5351	3.2612	3.3452	0.98
16	2.4678	1.6514	5.4054	0.82	37	2.5443	3.2980	3.2461	0.98
17	2.4683	1.7980	5.3271	0.84	38	2.5544	3.3324	3.1485	0.98
18	2.4690	1.9336	5.2414	0.86	39	2.5655	3.3646	3.0527	0.99
19	2.4698	2.0592	5.1494	0.87	40	2.5776	3.3947	2.9584	0.99
20	2.4708	2.1757	5.0525	0.89	41	2.5908	3.4227	2.8655	0.99
21	2.4719	2.2840	4.9515	0.90	42	2.6052	3.4488	2.7740	0.99
22	2.4733	2.3847	4.8473	0.91	43	2.6208	3.4730	2.6835	0.99
23	2.4749	2.4784	4.7407	0.92	44	2.6377	3.4955	2.5939	0.99
24	2.4768	2.5658	4.6324	0.93	45	2.6561	3.5161	2.5049	0.99
25	2.4791	2.6474	4.5229	0.94	46	2.6760	3.5350	2.4160	0.99
26	2.4816	2.7235	4.4127	0.95	47	2.6974	3.5522	2.3268	0.99
27	2.4846	2.7947	4.3023	0.95	48	2.7205	3.5676	2.2368	0.99
28	2.4879	2.8612	4.1920	0.96	49	2.7454	3.5812	2.1454	0.99
29	2.4917	2.9235	4.0822	0.96	50	2.7721	3.5930	2.0519	0.99
30	2.4961	2.9817	3.9732	0.97					

in HH and VV polarizations, respectively, are shown as follows:

$$\begin{cases} A_{hh}\theta = 2.4929 - 0.3561 * \theta + 1.0596 * \theta^2 - 1.0179 * \theta^3 \\ B_{hh}\theta = -2.2455 + 19.6825 * \theta - 21.8263 * \theta^2 + 10.2729 * \theta^3 \\ C_{hh}(\theta) = 5.8102 + 0.9994 * \theta - 12.0484 * \theta^2 + 7.0650 * \theta^3 \end{cases} \quad (6)$$

$$\begin{cases} A_{vv}(\theta) = 2.4223 + 0.4130 * \theta - 1.2872 * \theta^2 + 1.4534 * \theta^3 \\ B_{vv}(\theta) = -2.2709 + 19.9188 * \theta - 24.4051 * \theta^2 + 10.6915 * \theta^3 \\ C_{vv}(\theta) = 5.7064 + 2.4551 * \theta - 15.9373 * \theta^2 + 9.6400 * \theta^3. \end{cases} \quad (7)$$

We present the final semiempirical model for soil moisture retrieval in C-band Envisat ASAR alternating polarization (AP) precision products. In order to obtain explicit equations for soil moisture and joint roughness parameter  $Z_s$ , as a function of backscattering coefficients for a specific incidence angle, we substitute formula (6) and (7) in HH and VV polarizations,

respectively, into (5). This leads to the following formulation:

$$\begin{cases} \sigma_{hh}^0(\theta) = A_{hh}(\theta) \text{Ln}(mv) + B_{hh}(\theta) \text{Ln}(Zs) + C_{hh}(\theta) \\ \sigma_{vv}^0(\theta) = A_{vv}(\theta) \text{Ln}(mv) + B_{vv}(\theta) \text{Ln}(Zs) + C_{vv}(\theta). \end{cases} \quad (8)$$

Solving (8) for  $\text{Ln}(mv)$  and  $\text{Ln}(Zs)$ , we can derive the final expression of soil moisture retrieval

$$mv(\theta) = \exp\left(\frac{B_{hh} * (\sigma_{vv}^0 - C_{vv}) - B_{vv} * (\sigma_{hh}^0 - C_{hh})}{B_{hh} * A_{vv} - B_{vv} * A_{hh}}\right). \quad (9)$$

Here, for simplicity and clarity, we omit the subscript  $\theta$  in the right-hand side of (9). However, it should be noted that two backscattering coefficients in HH and VV polarization modes, respectively, are required to determine soil moisture at a given incidence angle.

#### IV. RESULTS

##### A. Study Area and Data

The study area is situated in the North China Plain, which is an important region for economic crop cultivation, including wheat and corn. The objective of this study is to assess the potential of SAR soil moisture retrieval and hydrological application, such as drought and rainfall monitoring on agricultural issue in this region. To achieve this, 58 precision products acquired by Envisat ASAR in AP mode between 27 April, 2004, and 3 October, 2011, were used. The images include all swaths of Envisat ASAR and consist of 18 images in descending mode and 40 images in ascending mode (see Table V). These images are in the 1B level of products with the type of ASA\_APP\_1P, which are derived from Level 0 data collected during the sensor's AP mode. The images are multilook, ground range, narrow swath digital images, with each acquisition containing two coregistered images processed with corrections for antenna pattern and range spreading loss. Furthermore, the images have been transformed into ground range products to correct significant distortion in the range direction, a necessary step for intercomparison of radar images acquired with different sensors, even for images acquired by the same sensor but in different modes or processed with different processors. Fig. 4 illustrates the coverage of SAR images and three validation regions, each approximately  $25 \times 25 \text{ km}^2$  in size.

In SAR soil moisture retrieval, the ratio between the transmitted pulse's amplitude and the received echo is typically stored as digital numbers. To convert these values to calibrated backscattering coefficients required for soil moisture retrieval, radiometric calibration is necessary. More detailed information on this approach can be found in the documents provided by the ESA. During the processing stage, a "flat terrain" assumption is made since the local slope or incidence angle (referred to as local incidence angle) is not known [40]. To achieve precise absolute image calibration and obtain backscattering coefficients  $\sigma^0$ , an external digital elevation model (DEM) derived from Shuttle Radar Topography Mission (STRM) DEM 30sec products is utilized. This DEM helps to calculate the local incidence angle

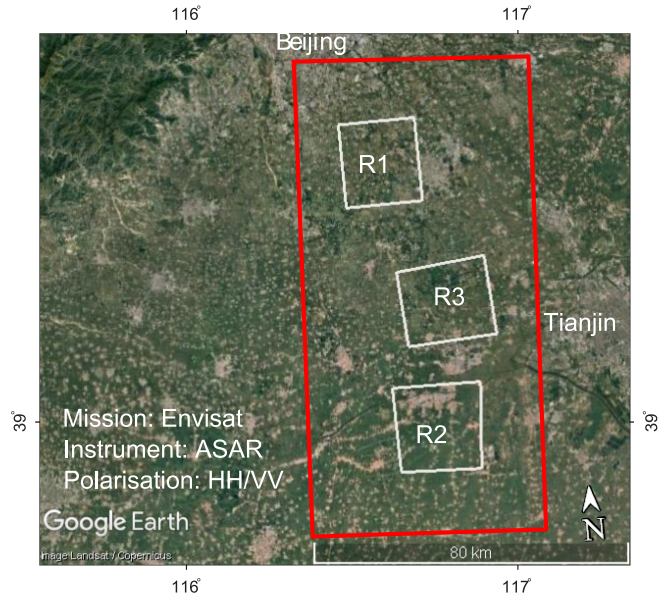


Fig. 4. Map of study area, locations of sample fields overlain on the Google Earth image (red box: SAR image coverage, including three validation regions, R1, R2, R3, background: Google Earth).

and implement terrain corrections to compensate for distortions caused by variations in topography and the sensor's tilt.

SAR images inherently contain speckles, which degrade image quality and impact feature interpretation. To mitigate the effects of speckles, a Lee sigma filter is employed with a patch window size of  $7 \times 7$  and a sigma threshold of 0.9 within a target window size of  $3 \times 3$ . Terrain correction is implemented using the range Doppler orthorectification method based on SRTM DEM. This correction compensates for distance distortions resulting from variations topography and the sensor's tilt [41].

To calculate soil moisture for each pixel in the image, processed SAR images and associated by-products, such as local incidence angle, are utilized during the range Doppler terrain correction process. The soil moisture is expressed in volume soil moisture measurements, with unit of  $\text{m}^3/\text{m}^3$ , ranging from 0 to 1. Soil moisture values exceeding 0.55 are masked out, primarily due to speckle noise or limitations of the inversion model.

##### B. Result and Validation

The proposed method allows for the retrieval of soil moisture from the pre-processed Envisat ASAR images. In this study, four different scenes of soil moisture derived from SAR images acquired on 3 April, 17 July, 2 October, and 20 December in 2005 were analyzed to demonstrate the seasonal variations in soil moisture. The results indicate significant seasonal changes, with average soil moisture values in region 1 of  $0.15 \pm 0.10$ ,  $0.29 \pm 0.10$ ,  $0.20 \pm 0.09$ , and  $0.14 \pm 0.10 \text{ m}^3/\text{m}^3$  in spring, summer, fall, and winter seasons, respectively (see Fig. 5). In the summer season, higher soil moisture levels are generally observed [see Fig. 5(b) and (f)], likely due to the influence of

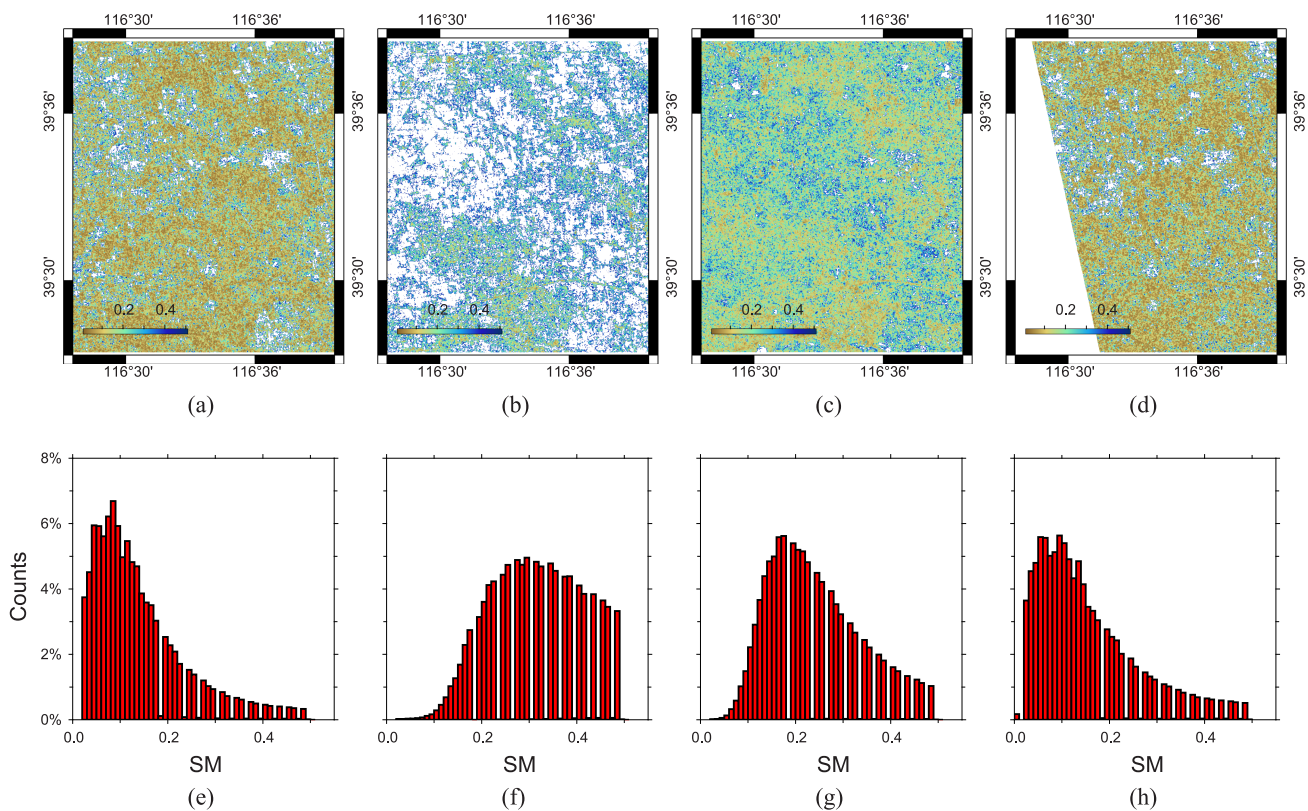


Fig. 5. Soil moisture derived from Envisat ASAR in region 1 acquired on (a), (e) 3 April, 2005, (b), (f) 17 July, 2005, (c), (g) 2 October, 2005, and (d), (h) 20 December, 2005, respectively.

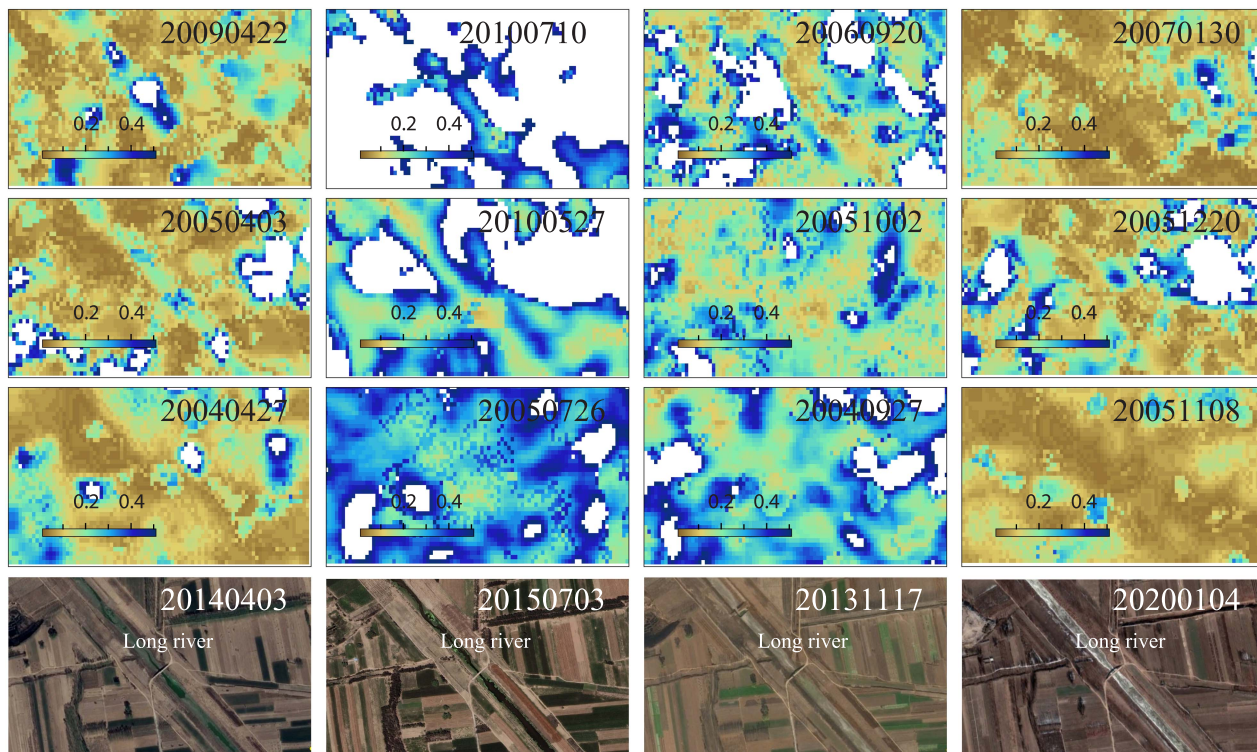


Fig. 6. Some examples of the soil moisture from Envisat ASAR grouped by seasons. The plots in first three rows expressed soil moisture contents from Envisat ASAR acquired on specific date grouped in seasons in columns (first col: spring, second col: summer, third col: fall, fourth col: winter). The last row shows the optical images on specific date from Google Earth.

TABLE V  
DETAILS OF ENVISAT ASAR AP IMAGES

No.	mode	swath	pass	acquired date	orbit/track
1	HH/VV	IS7	Ascending	27-Apr-2004	11 287/211
2	HH/VV	IS7	Ascending	27-Apr-2004	11 287/211
3	HH/VV	IS7	Ascending	1-Jun-2004	11 788/211
4	HH/VV	IS7	Ascending	1-Jun-2004	11 788/211
5	HH/VV	IS4	Ascending	27-Sep-2004	13 477/397
6	HH/VV	IS3	Descending	17-Oct-2004	13 756/175
7	HH/VV	IS2	Ascending	3-Apr-2005	16 168/82
8	HH/VV	IS7	Descending	4-Apr-2005	16 175/89
9	HH/VV	IS7	Ascending	12-Apr-2005	16 297/211
10	HH/VV	IS7	Ascending	12-Apr-2005	16 297/211
11	HH/VV	IS2	Descending	13-Apr-2005	16 304/218
12	HH/VV	IS2	Descending	13-Apr-2005	16 304/218
13	HH/VV	IS2	Ascending	17-Jul-2005	17 671/82
14	HH/VV	IS3	Descending	24-Jul-2005	17 764/175
15	HH/VV	IS7	Ascending	26-Jul-2005	17 800/211
16	HH/VV	IS7	Ascending	26-Jul-2005	17 800/211
17	HH/VV	IS2	Ascending	21-Aug-2005	18 172/82
18	HH/VV	IS7	Ascending	30-Aug-2005	18 301/211
19	HH/VV	IS7	Ascending	30-Aug-2005	18 301/211
20	HH/VV	IS2	Descending	31-Aug-2005	18 308/218
21	HH/VV	IS2	Descending	31-Aug-2005	18 308/218
22	HH/VV	IS3	Descending	2-Oct-2005	18 766/175
23	HH/VV	IS7	Ascending	8-Nov-2005	19 303/211
24	HH/VV	IS1	Ascending	20-Dec-2005	19 904/311
25	HH/VV	IS2	Descending	20-Sep-2006	23 819/218
26	HH/VV	IS2	Descending	20-Sep-2006	23 819/218
27	HH/VV	IS2	Ascending	15-Oct-2006	24 184/82
28	HH/VV	IS3	Ascending	31-Jan-2007	25 730/125
29	HH/VV	IS3	Ascending	7-Mar-2007	26 231/125
30	HH/VV	IS1	Descending	26-May-2008	32 608/490
31	HH/VV	IS1	Descending	26-May-2008	32 608/490
32	HH/VV	IS7	Ascending	15-Jul-2008	33 331/211
33	HH/VV	IS7	Ascending	15-Jul-2008	33 331/211
34	HH/VV	IS6	Ascending	31-Jul-2008	33 560/440
35	HH/VV	IS6	Ascending	31-Jul-2008	33 560/440
36	HH/VV	IS4	Ascending	1-Sep-2008	34 018/397
37	HH/VV	IS6	Ascending	9-Oct-2008	34 562/440
38	HH/VV	IS6	Ascending	9-Oct-2008	34 562/440
39	HH/VV	IS7	Ascending	28-Oct-2008	34 834/211
40	HH/VV	IS7	Ascending	28-Oct-2008	34 834/211
41	HH/VV	IS2	Descending	22-Apr-2009	37 346/218
42	HH/VV	IS1	Descending	22-Apr-2009	37 346/218
43	HH/VV	IS6	Ascending	7-May-2009	37 568/440
44	HH/VV	IS6	Ascending	7-May-2009	37 568/440
45	HH/VV	IS2	Ascending	17-May-2009	37 711/82
46	HH/VV	IS2	Descending	27-May-2009	37 847/218
47	HH/VV	IS2	Descending	27-May-2009	37 847/218
48	HH/VV	IS4	Ascending	8-Jun-2009	38 026/397
49	HH/VV	IS6	Ascending	11-Jun-2009	38 069/440
50	HH/VV	IS6	Ascending	11-Jun-2009	38 069/440
51	HH/VV	IS6	Ascending	27-May-2010	43 079/440
52	HH/VV	IS6	Ascending	27-May-2010	43 079/440
53	HH/VV	IS6	Ascending	1-Jul-2010	43 580/440
54	HH/VV	IS6	Ascending	1-Jul-2010	43 580/440
55	HH/VV	IS6	Ascending	5-Aug-2010	44 081/440
56	HH/VV	IS6	Ascending	5-Aug-2010	44 081/440
57	HH/VV	IS1	Descending	3-Oct-2011	50 161/147
58	HH/VV	IS1	Descending	3-Oct-2011	50 161/147

rainfall. This is evident from relatively heavy rainfall event of 11 mm on 16 July, which contributes to increased soil moisture content. However, excessive water content in the soil resulting from rainfall may lead to failure in soil moisture retrieval [see Fig. 5(b)]. The remaining two regions exhibit similar seasonal change patterns.

To further investigate the seasonal variations in soil moisture, a smaller region situated in LangFang city was selected (see Fig. 6). This region includes a river called Long River, a seasonal river that flows from northwest to southeast. In spring and summer, the region is covered by crops or trees. However, in the fall winter seasons, the region appears either bare or has sparse crop coverage.

The first three rows in Fig. 6 depict soil moisture on different dates, divided into seasons in column modes. The last row displays corresponding images acquired during different seasons. Noted that soil moisture on 8 November, 2005, is also categorized as winter due to the absence of acquisitions during that season. The last row in Fig. 6 shows the corresponding images acquired on different seasons. Upon visual inspection, it is evident that the surface exhibits greater vegetation cover during summer and fall, while spring and winter show less vegetation. Soil moisture appears to be wetter during the summer compared with the other seasons, and heavy rainfall or man-made irrigation may be key factors influencing soil moisture dynamics. Notably, on 10 July, 2010, the soil moisture is notably higher compared

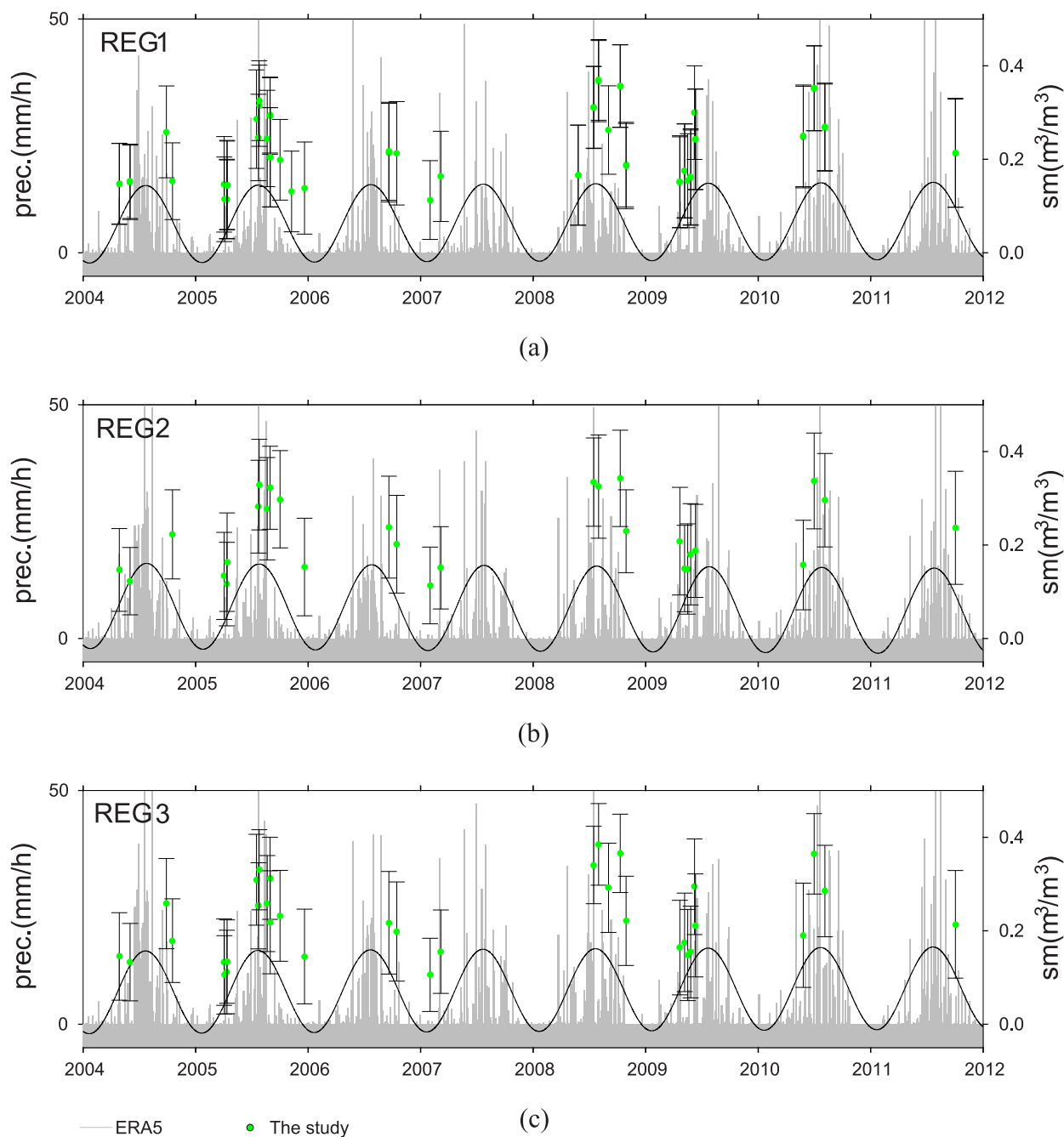


Fig. 7. SAR-derived soil moisture and hourly precipitation from ERA5-land products. (a) Region 1. (b) Region 2. (c) Region 3.

with other dates, which can be attributed to significant rainfall events on 9 and 10 July, with precipitation amounts of 10.3 and 2.2 mm, respectively. This high soil moisture level resulted in difficulties in retrieving soil moisture in several regions. The soil moisture in Long River area shows pronounced seasonal changes. During summer and winter, the soil moisture in the river does not exhibit significant differences compared with the surrounding regions. However, in spring, a noticeable disparity emerges, indicating that the river area has higher soil moisture compared with the rest of the areas. The absence of an obvious difference pattern between the river and other regions may be due to the nearly dry conditions in winter or the abundant water in

summer, while the river maintains higher moisture levels during spring.

We conducted further investigations into the relationship between all soil moistures and rainfall using hourly ECMWF's ERA5 land product (see Fig. 7). The soil moisture in three regions exhibits a clear seasonal pattern during the summer season than during the other seasons. The average soil moisture value in summer exceeds  $0.2 \text{ m}^3/\text{m}^3$ , indicating a wetter soil condition influenced by frequent heavy rainfall (see Fig. 7). In specific year, such as 2005 and 2008, the average soil moisture during the summer season is higher compared with other summer seasons due to the occurrence of frequent



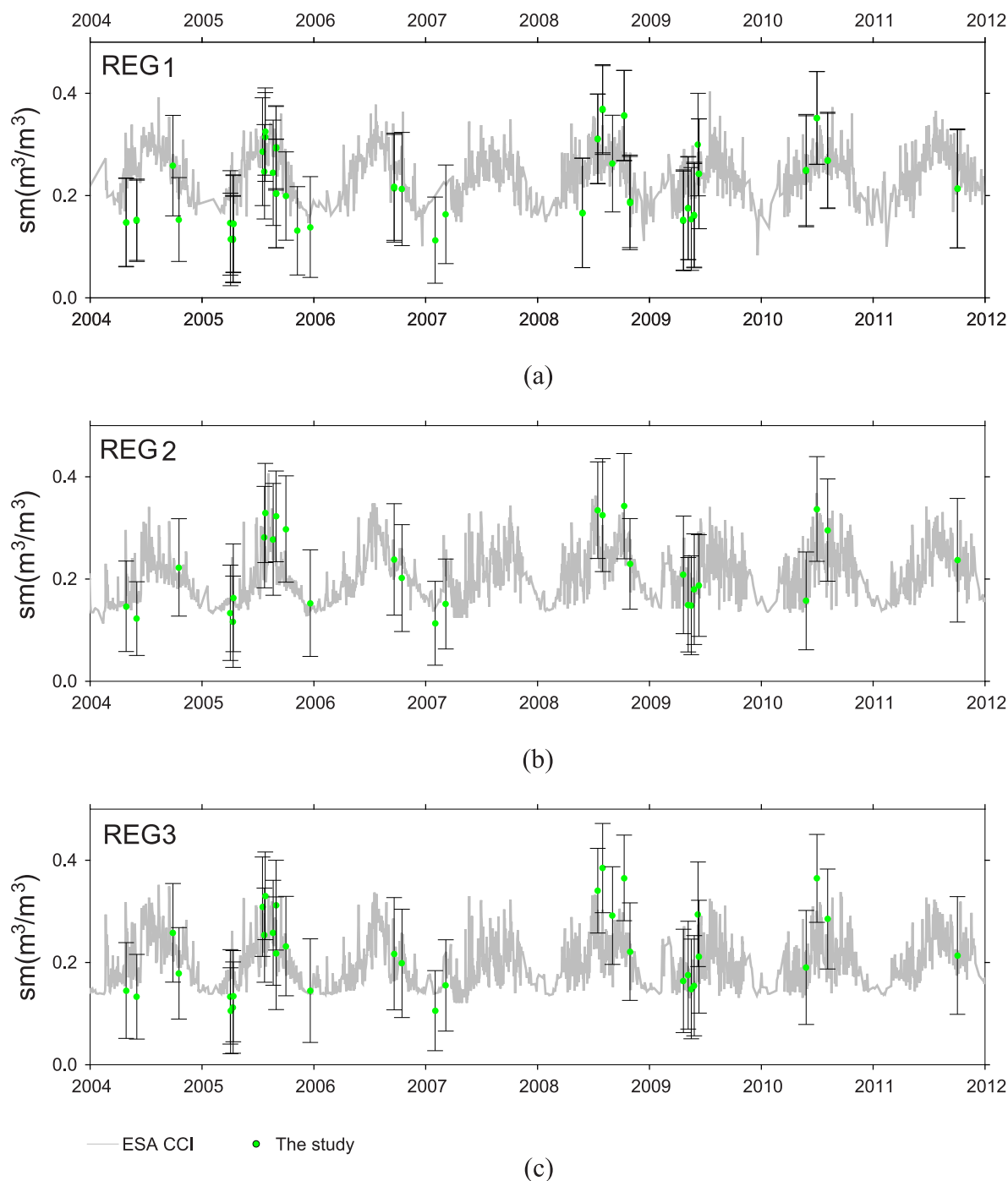


Fig. 8. SAR-derived soil moisture and ESA CCI daily soil moisture data products. (a) Region 1. (b) Region 2. (c) Region 3.

heavy rainfall events exceeding 30 mm. For instance, a heavy rainfall event on 23 July, 2005, resulted in a total precipitation of 77.4 mm, with the highest soil moisture recorded as  $0.33 \pm 0.09 \text{ m}^3/\text{m}^3$  on 26 July. The seasonal change in soil moisture observed in the SAR-derived soil moisture products align with those observed in the ESA CCI and ERA5 land soil moisture products (see Figs. 8 and 9). Notably, there is a strong relationship between soil moisture and rainfall events. These show that rainfall is a significant factor influencing soil moisture dynamics.

It is worth noting that the region experienced extreme drought events during the analyzed period. These events were characterized by a prolonged lack rainfall for several months, resulting in soil moisture levels approaching or falling below the threshold for dry soil (close to or below  $0.1 \text{ m}^3/\text{m}^3$ ). At least two extreme drought events occurred in the region during the study period, one between November 2004 and April 2005 and another between December 2008 and May 2009. During the spring seasons of 2005 and 2009, the SAR-derived soil moisture values were within the range of  $0.1 \pm 0.02$  and  $0.15 \pm 0.02 \text{ m}^3/\text{m}^3$ ,

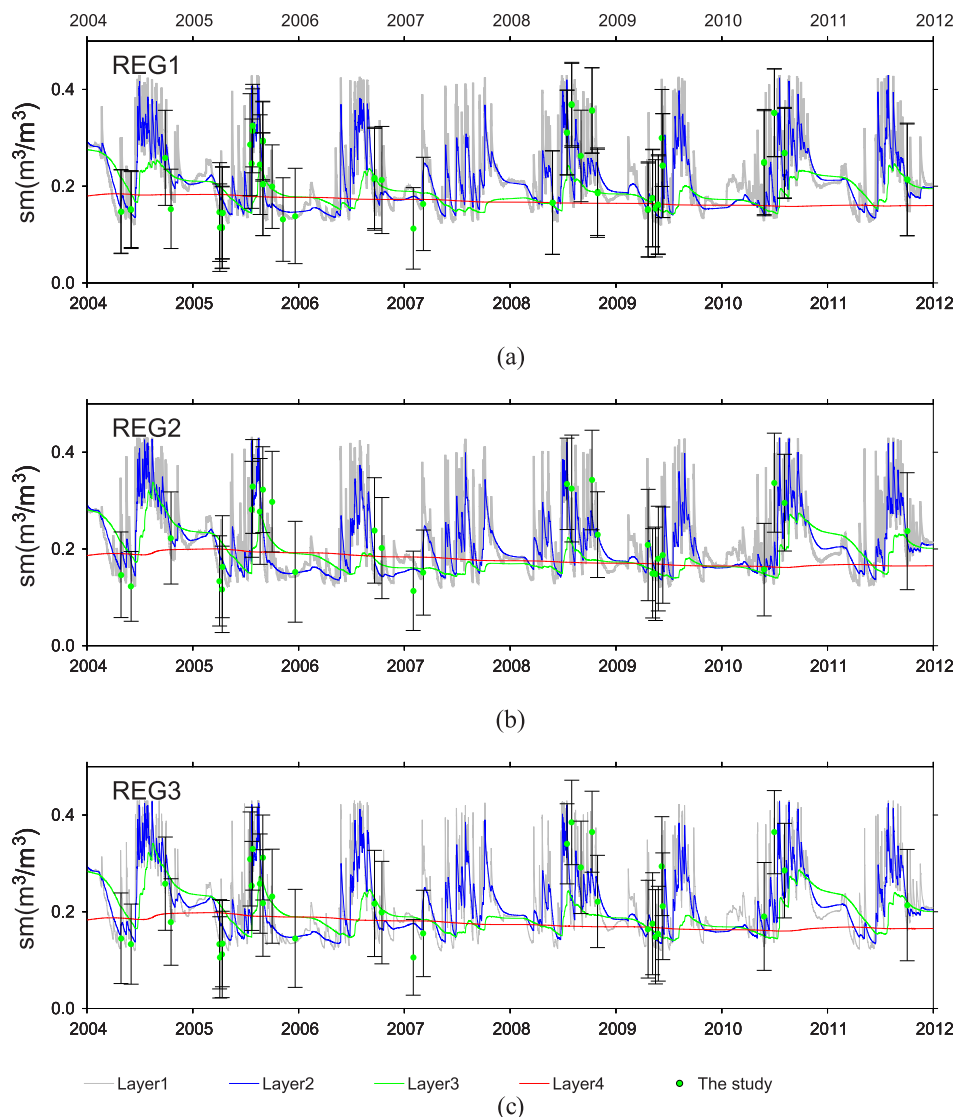


Fig. 9. SAR-derived soil moisture and ERA5-land reanalysis hourly products. (a) Region 1. (b) Region 2. (c) Region 3.

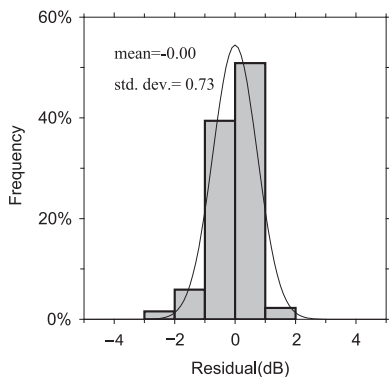


Fig. 10. Distribution of residual.

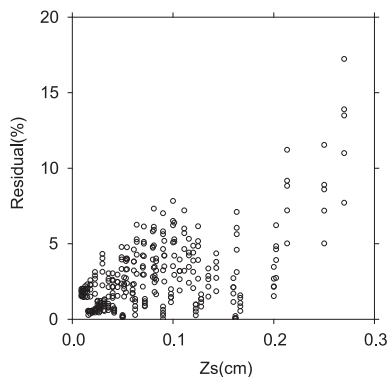


Fig. 11. Relative errors of the prediction.

respectively, indicating near-dry soil conditions ( $<0.1 \text{ m}^3/\text{m}^3$ ). However, the soil moisture during the period did not significantly differ from the corresponding period in the other years. Some measures were implemented to mitigate the impact of drought,

such as groundwater irrigation and artificial precipitation. Overall, this study highlights the importance of monitoring and understanding soil moisture dynamics, particularly in regions prone to drought and other extreme weather events.

To validate SAR-derived soil moisture, we compared it with the ESA CCI soil moisture (ESA CCI SM v07.1) [25], [26] and reanalysis soil moisture from ERA5 hourly land product [28]. The ESA CCI soil moisture product incorporates soil moisture data retrieved from 17 active and passive microwave satellite sensors from 1978 to 2021, whereas the ECMWF ERA5-Land product provides hourly surface variable information with a horizontal resolution of  $0.1^\circ \times 0.1^\circ$ . We assessed the performance of the SAR-derived soil moisture by comparing it with the daily ESA CCI soil moisture products, which have a spatial resolution of  $0.25^\circ \times 0.25^\circ$  (see Fig. 8). The accuracy of ESA CCI soil moisture product is  $\sim 0.06 \text{ m}^3/\text{m}^3$  [42]. In the three validation regions throughout the entire study period, the mean and standard deviation of differences between two soil moisture products are  $-0.03 \pm 0.05$ ,  $0.0 \pm 0.05$ , and  $0.0 \pm 0.05 \text{ m}^3/\text{m}^3$ , respectively. The corresponding correlation coefficients of two soil moisture dataset are 0.80, 0.82, and 0.80, respectively, indicating good consistency. Although the SAR-derived soil moisture in region 1 is slightly lower than that of the ESA CCI soil moisture contents, the differences between two data only account for approximately 10% of the soil moisture values. The slight differences may be attributed to different spatial resolutions and uncertainties of the two datasets.

Furthermore, we examined the performance of SAR-derived the soil moisture compared with ECMWF's ERA5-Land soil moisture dataset. The accuracy of the ERA5-Land soil moisture is about  $\sim 0.05 \text{ m}^3/\text{m}^3$  [43]. The ERA5 soil moisture data product provides estimates for soil moisture in four layers corresponding to depths of 0–7, 2–28, 28–100, and 100–289 cm. In region 1, the mean and standard deviation of differences between the retrieved soil moisture and ERA5-Land soil moisture are  $0 \pm 0.06$ ,  $0.01 \pm 0.07$ , and  $0.02 \pm 0.08 \text{ m}^3/\text{m}^3$  for Layers 1–3, respectively. Layer 4 is excluded as there is no variation in soil moisture (see Fig. 9). In region 2, the differences have mean and standard deviation of  $-0.02 \pm 0.06$ ,  $-0.01 \pm 0.07$ , and  $0.02 \pm 0.09 \text{ m}^3/\text{m}^3$ , respectively. In region 3, the differences are  $-0.02 \pm 0.06$ ,  $0.01 \pm 0.08$ , and  $0.01 \pm 0.09 \text{ m}^3/\text{m}^3$  for mean and standard deviation, respectively. We compared the ERA5-Land soil moisture products within 1–2 h of the Envisat ASAR observation time for the comparison. Overall, the differences between two soil moisture products demonstrate good consistency. The SAR-derived soil moisture is more compatible with the ERA5-Land soil moisture in layer 1 because the SAR signal only penetrates a relative shallow layer [44].

## V. DISCUSSION

Although many studies have evaluated the performance of soil dielectric models, such as Wang–Schmugge, Mironov, Dobson, and four-phase on different microwave bands and modes (passive or active) [23], [45], [46], the soil dielectric model is crucial for accuracy and performances of soil moisture retrieval. In this study, we also investigated the effect of soil dielectric mixing models on soil moisture retrieval using Hillikaninen and Mironov models at C-band active SAR. We selected two scenes of Envisat ASAR acquired on 27 April, 2004 (spring), and 26 July 26, 2005 (summer), to evaluate the performances of

dielectric models. The mean and standard deviation of soil moisture in region 1 are  $0.11 \pm 0.08$  and  $0.15 \pm 0.09 \text{ m}^3/\text{m}^3$  for Hillikaninen and Mironov models on 27 April, 2004, and  $0.31 \pm 0.09 \text{ m}^3/\text{m}^3$  and  $0.28 \pm 0.08 \text{ m}^3/\text{m}^3$ , respectively, on 26 July, 2005. The errors induced by different dielectric models is about  $0.035 \text{ m}^3/\text{m}^3$  in the both cases, which is equivalent to 1%–2.7% of soil moisture and meets the standard accuracy requirement of about  $0.04 \text{ m}^3/\text{m}^3$  for dielectric models [47], [48]. The differences between two models are also within the uncertainty of each model itself, indicating no significant difference between models.

We assume that the influence of soil moisture [ $\text{Ln}(mv)$ ] and surface roughness [ $\text{Ln}(Z_s)$ ] on backscattering coefficient is uncorrelated, which is reasonable because the backscattering coefficients can be easily explained using a linear relation with  $\text{Ln}(Z_s)$  at different soil moisture level (see Figs. 2 and 3). This assumption allows us to estimate the sensitivity of backscattering coefficient to soil moisture and surface roughness independently. The uncertainty of the approach contributed by surface roughness ( $Z_s$ ) could be get in Fig. 3. Here, we calculated the residuals of backscattering coefficient caused by surface roughness ( $Z_s$ ) at an incidence angle of  $35^\circ$  at a wide range of soil moisture (5%–45%) (see Fig. 10). The mean and standard deviation of residuals were  $0 \pm 0.73 \text{ dB}$ , indicating a good characterization of the backscattering coefficients when utilizing surface roughness [ $\text{Ln}(Z_s)$ ]. The relative error (or proportional error), calculated as residual error divided by the backscattering coefficients, is also presented. The majority of residuals are below 15%, with over 90% of residuals being less than 5%. The larger residuals mainly occur on very rough surface (see Fig. 11). In addition, for fitted coefficients  $A(\theta)$ ,  $(\theta)$ , and  $C(\theta)$ , the residual of cubic model could be neglected from  $R^2$  test.

## VI. CONCLUSION

We conducted a comprehensive investigation of the backscattering coefficients in C-band (Envisat ASAR) in response to soil moisture contents and surface parameters using the AIEM model across a wide range of incidence angles. Our simulation results showed that there were exponential relations between backscattering coefficients and soil moisture and roughness. These relations could be described as polynomials of local incidence. Based on these relations, we proposed a new semiempirical algorithm for soil moisture retrieval, which was found to be a good approximation to the theoretical model for backscattering calculation in smooth and moderately rough surfaces.

We applied the proposed algorithm to an eight-year time series of predicted soil moisture contents over a broad region of northern China. Due to the lack of synchronous in-situ observational data for validation, we used ESA CCI soil moisture products and ERA5-Land hourly reanalysis products for comparison analysis. The results demonstrated good consistency, and the proposed algorithm was able to capture significant drought and rainfall events, highlighting the capability of the AIEM and Mironov dielectric model for soil moisture retrieval. However, further

validation of the model using observational measurements is necessary to estimate the absolute accuracy of the retrieval.

We did not consider the influence of vegetation on backscattering coefficients, which should be subtracted from the backscattering coefficient received by the satellite sensor for the real soil moisture. In addition, a relatively sparse sampling in the time period and changes in land use also hindered quantitative analysis in the time series to obtain more details information, such as the decomposition of seasonal effects in long-term trend study. Overcoming the issue of sparse time sampling can be achieved through the utilization of SAR platforms with high repeat frequency. In conclusion, our study sheds new light on the hydrological issue using space-borne SAR-based retrieval techniques for soil moisture content.

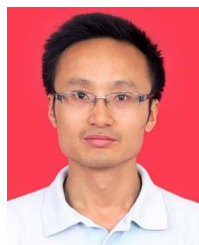
#### ACKNOWLEDGMENT

The authors would like to thank Prof. K. S. C. and Z. L. affiliated in Aerospace Information Research Institute, Chinese Academy of Sciences, for the help and support for AIEM model.

#### REFERENCES

- [1] C. Pathe, W. Wagner, D. Sabel, M. Doubkova, and J. B. Basara, "Using ENVISAT ASAR global mode data for surface soil moisture retrieval over Oklahoma, USA," *IEEE Trans. Geosci. Remote Sens.*, vol. 47, no. 2, pp. 468–480, Feb. 2009, doi: [10.1109/TGRS.2008.2004711](https://doi.org/10.1109/TGRS.2008.2004711).
- [2] J. P. Walker, G. R. Willgoose, and J. D. Kalma, "In situ measurement of soil moisture: A comparison of techniques," *J. Hydrol.*, vol. 293, no. 1–4, pp. 85–99, 2004, doi: [10.1016/j.jhydrol.2004.01.008](https://doi.org/10.1016/j.jhydrol.2004.01.008).
- [3] S. P. Kovach, "Methods of measuring the soil-moisture status in the field," *Plant Physiol.*, vol. 63, no. 5, 1979, Art. no. 89.
- [4] S. U. Susha Lekshmi, D. N. Singh, and M. Shojaei Baghini, "A critical review of soil moisture measurement," *Measurement*, vol. 54, pp. 92–105, Aug. 2014, doi: [10.1016/j.measurement.2014.04.007](https://doi.org/10.1016/j.measurement.2014.04.007).
- [5] A. Robock et al., "The global soil moisture data bank," *Bull. Meteorol. Soc.*, vol. 81, no. 6, pp. 1281–1300, 2000.
- [6] A. Merzouki, H. McNairn, and A. Pacheco, "Mapping soil moisture using RADARSAT-2 data and local autocorrelation statistics," *IEEE J. Sel. Topics Appl. Earth Observ. Remote Sens.*, vol. 4, no. 1, pp. 128–137, Mar. 2011, doi: [10.1109/Jstars.2011.2116769](https://doi.org/10.1109/Jstars.2011.2116769).
- [7] H. Wang et al., "Increased water storage in North America and scandinavia from GRACE gravity data," *Nature Geosci.*, vol. 6, no. 1, pp. 38–42, 2012, doi: [10.1038/NNGEO1652](https://doi.org/10.1038/NNGEO1652).
- [8] E. G. Njoku and J. A. Kong, "Theory for passive microwave remote-sensing of near-surface soil-moisture," *J. Geophys. Res.*, vol. 82, no. 20, pp. 3108–3118, 1977.
- [9] E. G. Njoku, "Theory for passive microwave remote-sensing of near-surface soil-moisture," *J. Geophys. Res.*, vol. 82, no. 20, pp. 3108–3118, 1977.
- [10] E. G. Njoku and D. Entekhabi, "Passive microwave remote sensing of soil moisture," *J. Hydrol.*, vol. 184, no. 1/2, pp. 101–129, Oct. 1996, doi: [10.1016/0022-1694\(95\)02970-2](https://doi.org/10.1016/0022-1694(95)02970-2).
- [11] J. Peng and A. Loew, "Recent advances in soil moisture estimation from remote sensing," *Water*, vol. 9, no. 7, 2017, Art. no. 530, doi: [10.3390/w9070530](https://doi.org/10.3390/w9070530).
- [12] A. Loew, R. Ludwig, and W. Mauser, "Derivation of surface soil moisture from ENVISAT ASAR wide swath and image mode data in agricultural areas," *IEEE Trans. Geosci. Remote Sens.*, vol. 44, no. 4, pp. 889–899, Apr. 2006, doi: [10.1109/Tgrs.2005.863858](https://doi.org/10.1109/Tgrs.2005.863858).
- [13] T. Tadono, M. Shimada, H. Fujii, and I. Kaihotsu, "Estimation and validation of soil moisture using PALSAR onboard ALOS over Mongolian plateau," in *Proc. Piers*, 2008, pp. 253–256.
- [14] T. J. Pultz, J. Sokol, B. Brisco, R. J. Brown, and Q. H. J. Gwyn, "Soil moisture estimation with RADARSAT," *Earth Surf. Remote Sens.*, vol. 3222, pp. 143–148, 1997.
- [15] I. Gherboudj, R. Magagi, A. A. Berg, and B. Toth, "Soil moisture retrieval over agricultural fields from multi-polarized and multi-angular RADARSAT-2 SAR data," *Remote Sens. Environ.*, vol. 115, no. 1, pp. 33–43, 2011, doi: [10.1016/j.rse.2010.07.011](https://doi.org/10.1016/j.rse.2010.07.011).
- [16] M. Kseneman and D. Gleich, "Comparison between Dubois and Shi empirical models used for soil moisture estimation for TerraSAR-X data," *Informacije Midem-J. Microelectronics Electron. Compon. Mater.*, vol. 40, no. 3, pp. 241–248, 2010.
- [17] M. Aubert et al., "Analysis of TerraSAR-X data sensitivity to bare soil moisture, roughness, composition and soil crust," *Remote Sens. Environ.*, vol. 115, no. 8, pp. 1801–1810, 2011, doi: [10.1016/j.rse.2011.02.021](https://doi.org/10.1016/j.rse.2011.02.021).
- [18] Y. H. Kerr, P. Waldteufel, J.-P. Wigneron, J. Martinuzzi, J. Font, and M. Berger, "Soil moisture retrieval from space: The soil moisture and Ocean salinity (SMOS) mission," *IEEE Trans. Geosci. Remote Sens.*, vol. 39, no. 8, pp. 1729–1735, Aug. 2001.
- [19] P. Beckmann and A. Spizzichino, *The Scattering of Electromagnetic Waves From Rough Surfaces*. Norwood, MA, USA: Artech House, 1987.
- [20] T. C. B. Schut, G. Hesselink, B. G. D. Grooth, and J. Greve, "Experimental and theoretical investigations on the validity of the geometrical optics model for calculating the stability of optical traps," *Cytometry*, vol. 12, no. 6, pp. 479–485, 1991.
- [21] F. T. Ulaby, R. K. Moore, and A. K. Fung, *Microwave Remote Sensing: Active and Passive. Volume II. Radar Remote Sensing and Surface Scattering and Emission Theory*. Reading, MA, USA: Addison-Wesley, 1982.
- [22] A. K. Fung and K. S. Chen, *Microwave scattering and emission models and their applications*. Boston, MA, USA: Artech House, 1994.
- [23] M. C. Dobson, F. T. Ulaby, M. T. Hallikainen, and M. A. El-Rayes, "Microwave dielectric behavior of wet soil-Part II: Dielectric mixing models," *IEEE Trans. Geosci. Remote Sens.*, vol. GE-23, no. 1, pp. 35–46, Jan. 1985, doi: [10.1109/TGRS.1985.289498](https://doi.org/10.1109/TGRS.1985.289498).
- [24] K. Chen, Z. Li, and Y. Liu, "Model analysis of bistatic scattering from randomly rough surfaces," *Beijing Hangkong Hangtian Daxue Xuebao/J. Beijing Univ. Aeronaut. Astronaut.*, vol. 41, no. 10, 2015, Art. no. 1765, doi: [10.13700/j.bh.1001-5965.2015.0205](https://doi.org/10.13700/j.bh.1001-5965.2015.0205).
- [25] W. Dorigo et al., "ESA CCI soil moisture for improved earth system understanding: State-of-the art and future directions," *Remote Sens. Environ.*, vol. 203, pp. 185–215, Dec. 2017, doi: [10.1016/j.rse.2017.07.001](https://doi.org/10.1016/j.rse.2017.07.001).
- [26] A. Gruber, T. Scanlon, R. van der Schalie, W. Wagner, and W. Dorigo, "Evolution of the ESA CCI soil moisture climate data records and their underlying merging methodology," *Earth Syst. Sci. Data*, vol. 11, pp. 717–739, 2019, doi: [10.5194/essd-11-717-2019](https://doi.org/10.5194/essd-11-717-2019).
- [27] W. Preimesberger, T. Scanlon, C.-H. Su, A. Gruber, and W. Dorigo, "Homogenization of structural breaks in the global ESA CCI soil moisture multisatellite climate data record," *IEEE Trans. Geosci. Remote Sens.*, vol. 59, no. 4, pp. 2845–2862, Apr. 2021, doi: [10.1109/TGRS.2020.3012896](https://doi.org/10.1109/TGRS.2020.3012896).
- [28] J. Muñoz-Sabater et al., "ERA5-land: A state-of-the-art global reanalysis dataset for land applications," *Earth Syst. Sci. Data*, vol. 13, no. 9, pp. 4349–4383, 2021, doi: [10.5194/essd-13-4349-2021](https://doi.org/10.5194/essd-13-4349-2021).
- [29] Y. Oh, K. Sarabandi, and F. T. Ulaby, "Semi-empirical model of the ensemble-averaged differential Mueller matrix for microwave backscattering from bare soil surfaces," *IEEE Trans. Geosci. Remote Sens.*, vol. 40, no. 6, pp. 1348–1355, Jun. 2002, doi: [10.1109/Tgrs.2002.800232](https://doi.org/10.1109/Tgrs.2002.800232).
- [30] P. C. Dubois, J. van Zyl, and T. Engman, "Measuring soil-moisture with imaging radars," *IEEE Trans. Geosci. Remote Sens.*, vol. 33, no. 4, pp. 915–926, Jul. 1995.
- [31] K. C. Kornelsen and P. Coulibaly, "Advances in soil moisture retrieval from synthetic aperture radar and hydrological applications," *J. Hydrol.*, vol. 476, pp. 460–489, 2013, doi: [10.1016/j.jhydrol.2012.10.044](https://doi.org/10.1016/j.jhydrol.2012.10.044).
- [32] T.-D. Wu and K.-S. Chen, "A reappraisal of the validity of the IEM model for backscattering from rough surfaces," *IEEE Trans. Geosci. Remote Sens.*, vol. 42, no. 4, pp. 743–753, Apr. 2004, doi: [10.1109/Tgrs.2003.815405](https://doi.org/10.1109/Tgrs.2003.815405).
- [33] H.-W. Lee, K.-S. Chen, T.-D. Wu, J.-S. Lee, J.-C. Shi, and J.-C. Wang, "Extension of advanced integral equation model for calculations of fully polarimetric scattering coefficient from rough surface," in *Proc. IEEE Int. Geosci. Remote Sens. Symp.*, 2007, pp. 365–368.
- [34] T.-D. Wu, K.-S. Chen, J. Shi, H.-W. Lee, and A. K. Fung, "A study of an AIEM model for bistatic scattering from randomly rough surfaces," *IEEE Trans. Geosci. Remote Sens.*, vol. 46, no. 9, pp. 2584–2598, Sep. 2008, doi: [10.1109/Tgrs.2008.919822](https://doi.org/10.1109/Tgrs.2008.919822).
- [35] N. Baghdadi and M. Zribi, "Evaluation of radar backscatter models IEM, OH and Dubois using experimental observations," *Int. J. Remote Sens.*, vol. 27, no. 18, pp. 3831–3852, 2006, doi: [10.1080/01431160600658123](https://doi.org/10.1080/01431160600658123).

- [36] G. Macelloni, G. Nesti, P. Pampaloni, S. Sigismondi, D. Tarchi, and S. Lolli, "Experimental validation of surface scattering and emission models," *IEEE Trans. Geosci. Remote Sens.*, vol. 38, no. 1, pp. 459–469, Jan. 2000.
- [37] F. Koudogbo, P. F. Combes, and H. J. Mametsa, "Numerical and experimental validations of IEM for bistatic scattering from natural and manmade rough surfaces," *Prog. Electromagn. Res.*, vol. 46, pp. 203–244, 2004.
- [38] M. Zribi and M. Dechambre, "A new empirical model to inverse soil moisture and roughness using two radar configurations," in *Proc. Geosci. Remote Sens. Symp.*, 2002, vol. 4, pp. 2223–2225.
- [39] J. Z. Wang, Y. S. Bao, Y. J. Zhang, J. J. Qu, and W. M. Zhang, "Soil moisture inversion using multi-polarization and multi-angle ENVISAT ASAR data in surface soils of bare area and wheat-covered area," *Trans. Chin. Soc. Agricultural Eng.*, vol. 26, no. 6, p. 205–210, 2010.
- [40] B. Rosich and P. Meadows, "Absolute calibration of ASAR level 1 products," 2004.
- [41] D. Small et al., "ASAR level 1 geolocation," in *Proc. ENVISAT Calibration Rev.*, ESA-ESTEC, Noordwijk, The Netherlands, 2002, pp. 1–8.
- [42] EODC, "ESA climate change initiative plus soil moisture," Earth Observation Data Centre for Water Resources Monitoring (EODC) GmbH, 2022. [Online]. Available: [https://www.esa-soilmoisture-cci.org/sites/default/files/documents/public/CCI%20SM%20v07.1%20documentation/ESA\\_CCI\\_SM\\_RD\\_D4.2\\_v3\\_Product\\_Users\\_Guide\\_v07.1\\_i1.0.pdf](https://www.esa-soilmoisture-cci.org/sites/default/files/documents/public/CCI%20SM%20v07.1%20documentation/ESA_CCI_SM_RD_D4.2_v3_Product_Users_Guide_v07.1_i1.0.pdf)
- [43] R. An et al., "Validation of the ESA CCI soil moisture product in China," *Int. J. Appl. Earth Observ. Geoinf.*, vol. 48, pp. 28–36, 2016, doi: [10.1016/j.jag.2015.09.009](https://doi.org/10.1016/j.jag.2015.09.009).
- [44] J. Beale, T. Waive, J. Evans, and R. Corstanje, "A method to assess the performance of SAR-derived surface soil moisture products," *IEEE J. Sel. Topics Appl. Earth Observ. Remote Sens.*, vol. 14, pp. 4504–4516, 2021, doi: [10.1109/JSTARS.2021.3071380](https://doi.org/10.1109/JSTARS.2021.3071380).
- [45] R. Liu, X. Wang, Z. Wang, and J. Wen, "Evaluating effects of dielectric models on the surface soil moisture retrieval in the Qinghai-Tibet plateau," *Sci. Cold Arid Regions*, vol. 13, no. 1, pp. 62–76, 2021, doi: [10.3724/SP.J.1226.2021.20067](https://doi.org/10.3724/SP.J.1226.2021.20067).
- [46] S. Suman, P. K. Srivastava, D. K. Pandey, R. Prasad, R. K. Mall, and P. O'Neill, "Comparison of soil dielectric mixing models for soil moisture retrieval using SMAP brightness temperature over croplands in India," *J. Hydrol.*, vol. 602, 2021, Art. no. 126673, doi: [10.1016/j.jhydrol.2021.126673](https://doi.org/10.1016/j.jhydrol.2021.126673).
- [47] P. Guo, J. Shi, B. Gao, and H. Wan, "Evaluation of errors induced by soil dielectric models for soil moisture retrieval at L-band," in *Proc. IEEE Int. Geosci. Remote Sens. Symp.*, 2016, pp. 1679–1682, doi: [10.1109/IGARSS.2016.7729429](https://doi.org/10.1109/IGARSS.2016.7729429).
- [48] P. K. Srivastava, P. O'Neill, M. Cosh, M. Kurum, R. Lang, and A. Joseph, "Evaluation of dielectric mixing models for passive microwave soil moisture retrieval using data from ComRAD ground-based SMAP simulator," *IEEE J. Sel. Topics Appl. Earth Observ. Remote Sens.*, vol. 8, no. 9, pp. 4345–4354, Sep. 2015, doi: [10.1109/JSTARS.2014.2372031](https://doi.org/10.1109/JSTARS.2014.2372031).



**Qiang Shen** received the B.S. degree in surveying and mapping engineering from the East China University of Technology, Jiangxi, China, in 2002, and the M.S. and Ph.D. degrees in geodesy and survey engineering from Wuhan University, Wuhan, China, in 2005 and 2008, respectively.

He is currently a Professor of the Innovation Academy for Precision Measurement Science and Technology, Chinese Academy of Sciences, Wuhan, China. His group is using a variety of remote sensing techniques to measure the movements of Earth's crust

and glacier, and retrieve surface parameters based on remote sensing (SAR and optical images), geodesy, and has contributed to understanding of surface movement, ice dynamics, and methodological advances. His research interests include understanding the deformation of Earth's crust, and ice dynamics of glacier, and retrieval of surface parameters inferred from SAR and optical images.



**Hansheng Wang** received the B.S. and M.S. degrees in applied geophysics from the China University of Geoscience, Wuhan, China, in 1984 and 1989, respectively, and the Ph.D. degree in solid geophysics from the Institute of Geodesy and Geophysics (IGG), Chinese Academy of Sciences (CAS), Wuhan, China, in 1999.

He is currently a Professor of Innovation Academy for Precision Measurement Science and Technology, CAS, working on space geodesy, glacial isostatic adjustment modeling, and hydrogeodesy.

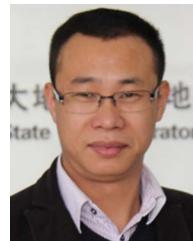


**C. K. Shum** received Ph.D. degree in aerospace engineering from The University of Texas at Austin, Austin, TX, USA, in 1982.

He is currently a Professor and Distinguished University Scholar with the Division of Geodetic Science, School of Earth Sciences, The Ohio State University, Columbus, OH, USA. He and his group focus on scientific research relating to the quantification of 20th Century and present-day global sea-level rise due to various geophysical sources, including anthropogenic climate-change. His research interests

include satellite geodesy, precision satellite orbit determination, temporal gravity field and tide modeling, and their cross-disciplinary science and applications to oceanography, hydrology, geodynamics, ice mass balance, GNSS meteorology, and space physics.

Dr. Shum is a Fellow of the American Association for the Advancement of Science (AAAS) and the International Association of Geodesy (IAG). He was the recipient of numerous awards including the 2012 Vening Meinesz Medal from the European Geosciences Union for distinguished research in Geodesy applied to sea-level science. He was a Lead Author for the Intergovernmental Panel for Climate Change (IPCC) Fourth Assessment Report (AR4), Working Group I, The Physical Science Basis. This contribution resulted in the 2007 Nobel Peace Prize jointly awarded to IPCC and Al Gore, Jr.



**Liming Jiang** received the B.S. degree in surveying and mapping engineering from Chang'an University, Xi'an, China, in 2000, the M.S. degree in remote sensing and GIS from the Chengdu University of Technology, Chengdu, China, in 2003, and the Ph.D. degree in photogrammetry and remote sensing from Wuhan University, Wuhan, China, 2006.

He is currently a Professor of the Innovation Academy for Precision Measurement Science and Technology, Chinese Academy of Sciences, Wuhan, China. He is also a Principal Investigator of one

project of the major program of National Natural Science Foundation of China (No. 41590854) named Lunar-Based Observation of Macro-Scale Dynamics of the Solid Earth: Mechanisms and Models. His research interests include imaging geodesy, InSAR methods and applications, and lunar-based SAR theory.



**Banghui Yang** received the B.S. degree in surveying and mapping engineering from the East China University of Technology, Jiangxi, China, in 2002, the M.S. degrees in geographic information system from Wuhan University, Wuhan, China, in 2005, and the Ph.D. degrees in Geographic information systems and Remote sensing from University of Chinese Academy of Sciences, Beijing, China in 2011.

He is currently an Associate Professor of Aerospace Information Research Institute, Chinese Academy of Sciences. His team is using a variety of

remote sensing technologies to develop application platforms for ecological protection, forestry, agriculture, and other industries. His research interests include remote sensing information extraction, target recognition, and 3-D simulation.



**Chaoyang Zhang** received the B.S. degree in geodesy and geomatics from Wuhan University, Wuhan, China, in 2015, and the Ph.D. in geodetic science from the Ohio State University, Columbus, OH, USA, in 2020.

He is currently a Research Associate with the University of Texas at Austin, Austin, TX, USA.



**Weiyu Lai** received the B.S. degree in surveying and mapping engineering from the Kunming University of Science and Technology, Kunming, China in 2020. She is currently working toward the M.S. degree in science and technology of surveying and mapping with the Innovation Academy for Precision Measurement Science and Technology, Chinese Academy of Sciences, Wuhan, China.

Her research interests include InSAR technology and its application.



**Jinlong Dong** received the B.S. degree in surveying and mapping engineering from Shandong Jianzhu University, Jinan, China, in 2014. He is currently working toward the Ph.D. degree in geodetic and surveying engineering with the Institute of Geodesy and Geophysics, Chinese Academy of Sciences, Wuhan, China, and the University of Chinese Academy of Sciences, Beijing, China.

His research interests include the lunar-based SAR interferometric theory and imaging geodesy.



**Tiantian Liu** received the B.S. degree in surveying and mapping engineering from the Changsha University of Science and Technology, Changsha, China, in 2021. She is currently working toward the M.S. degree in science and technology of surveying and mapping with the Innovation Academy for Precision Measurement Science and Technology, Chinese Academy of Sciences, Wuhan, China.

Her research interests include satellite altimetry data processing and glacier mass balance monitoring.



**Fan Gao** received the B.S. degree in surveying and mapping engineering from the Shandong University of Technology, Zibo, China, in 2018. She is currently working toward the Ph.D. in mapping science and technology, major in the numerical simulation about dynamics processes of Antarctica Ice Sheet, with the University of Chinese Academy of Sciences, Beijing, China.